

Thermoelectric properties of *p*-type CuInSe₂ chalcopyrites enhanced by introduction of manganese

Jinlei Yao,¹ Nathan J. Takas,^{2,3} Megan L. Schliefer,⁴ David S. Paprocki,⁴ Peter E. R. Blanchard,⁵ Huiyang Gou,⁶ Arthur Mar,⁵ Christopher L. Exstrom,⁴ Scott A. Darveau,⁴ Pierre F. P. Poudeu,^{2,3} and Jennifer A. Aitken^{1,*}

¹*Department of Chemistry and Biochemistry, Duquesne University, Pittsburgh, Pennsylvania 15282, USA*

²*Advanced Materials Research Institute, University of New Orleans, New Orleans, Louisiana 70148, USA*

³*Department of Chemistry, University of New Orleans, New Orleans, Louisiana 70148, USA*

⁴*Department of Chemistry, University of Nebraska Kearney, Kearney, Nebraska 68849, USA*

⁵*Department of Chemistry, University of Alberta, Edmonton, Alberta T6G 2G2, Canada*

⁶*State Key Laboratory of Metastable Materials Science and Technology, College of Material Science and Engineering, Yanshan University, Qinhuangdao 066004, China*

(Received 20 February 2011; revised manuscript received 27 May 2011; published 8 August 2011)

Thermoelectric properties, x-ray photoelectron spectroscopy, Raman spectroscopy, and electronic structures have been studied for Mn-substituted CuInSe₂ chalcopyrites. Raman spectroscopy verifies the lattice disorder due to the introduction of Mn into the CuInSe₂ matrix, leading to a slight suppression of thermal conductivity. On the other hand, the Mn substitution significantly increases the electrical conductivity and Seebeck coefficient. Therefore the thermoelectric figure of merit *ZT* has been enhanced by over two orders of magnitude by the introduction of Mn into CuInSe₂. These materials are *p*-type degenerate semiconductors, containing divalent Mn species as confirmed by x-ray photoelectron spectroscopy. The crystal structure of Mn-substituted CuInSe₂, as well as related ternary and quaternary diamond-like semiconductors, can be viewed as a combination of an electrically conducting unit, the Cu-Se and Mn-Se networks, and an electrically insulating unit, the In-Se network. Therefore, diamond-like semiconductors can serve as a potential class of thermoelectric materials with relatively wide band gaps upon substitution with Mn or other transition metals.

DOI: [10.1103/PhysRevB.84.075203](https://doi.org/10.1103/PhysRevB.84.075203)

PACS number(s): 72.20.Pa, 78.30.Fs

I. INTRODUCTION

Chalcopyrite compounds and their solid solutions have drawn considerable attention due to their potential technological applications, for example, in the areas of photovoltaic solar cells,¹ nonlinear optical devices,² etc. Chalcopyrites are ternary diamond-like semiconductors that crystallize in the noncentrosymmetric tetragonal space group *I*-42*d* [Fig. 1(a)]. There are two types of chalcopyrite semiconductors: $A^{II}B^{IV}X^{VI}_2$ ($A^{II} = \text{Cd, Zn, Hg}$; $B^{IV} = \text{Si, Ge, Sn}$; and $X^{VI} = \text{P, As, Sb}$) and $A^I B^{III} X^{VI}_2$ ($A^I = \text{Cu, Ag}$; $B^{III} = \text{Fe, Al, Ga, In, Tl}$; and $X^{VI} = \text{S, Se, Te}$), depending on the constituent elements.³ The chalcopyrite structure can be derived from that of the well-known zinc blende.⁴ The divalent cation of the $A^{II}X^{VI}$ zinc blende is replaced alternately with monovalent and trivalent cations, resulting in the chalcopyrite crystal structure. In this way, each anion is coordinated by two A^I and two B^{III} cations, whereas each cation is tetrahedrally coordinated by four anions. However, the existence of two different cations results in two unequal bond distances R_{A-X} and R_{B-X} , and hence yields two additional structural features compared with the zinc blende: (i) the chalcopyrite structure exhibits a tetragonal deformation with a distortion parameter $\eta = c/2a$, which can differ from its ideal value of one in the zinc blende, and (ii) the anions are slightly displaced from the ideal tetrahedral site by an amount of $|u - \frac{1}{4}|$, where u is the anion x coordinate. Although these structural differences relative to the zinc blende are small, the effects on the band structure and thus the physical properties are not negligible. In the Cu-based $A^I B^{III} X^{VI}_2$ chalcopyrites, for example, the *d*-*p* hybridization and anion displacement result in smaller band gaps than the binary zinc blende analogs.⁵⁻⁷

Although several members in the family of chalcopyrites and their derivatives have already been shown to demonstrate unique physical properties,^{1,2} studies on these compounds are still in progress in order to explore other useful properties.⁸⁻¹⁰ The purpose of this work is to propose a route to search for new bulk thermoelectric materials in Cu-based $A^I B^{III} X^{VI}_2$ chalcopyrites and related quaternary compounds, which complements the recent thermoelectric studies of $\text{Cu}_{2+x}B^{II}_{1-x}\text{Sn}X^{VI}_4$ ($B^{II} = \text{Zn, Cd}$ and $X^{VI} = \text{S, Se}$) stannites.¹¹ In pursuit of novel thermoelectric compounds, one of the best ideas is the phonon-glass, electron-crystal concept,¹² which envisions materials possessing high electron conductivity and mobility similar to crystalline materials, simultaneously with low thermal transport properties similar to a glass or amorphous solid. Validation of this concept was realized by the observation of a high figure of merit *ZT* for filled skutterudites and clathrates at high temperatures.^{13,14} Generally these well-known thermoelectric materials have narrow band gaps and high mobility,^{13,15-18} resulting in lower Seebeck coefficients *S* relative to wide-band-gap semiconductors. In this work, the thermoelectric material search is switched to the Cu-based chalcopyrites possessing relatively wide band gaps.⁴ The electronic band structure calculations of $A^I B^{III} X^{VI}_2$ ($A^I = \text{Cu, Ag}$; $B^{III} = \text{Al, Ga, In}$; and $X^{VI} = \text{S, Se}$) chalcopyrites reveal that the top of the valence band maximum (VBM) is mainly composed of $A^I d$ and $X^{VI} p$ orbitals. In contrast, hybridization of B^{III} and X^{VI} orbitals lies deep in the valence band and in the conduction band minimum (CBM).^{4,6,7} The hybridization of A^I and X^{VI} orbitals around the VBM can provide a conduction pathway for charge carriers in the *p*-type semiconductors, which makes the A^I-X^{VI}

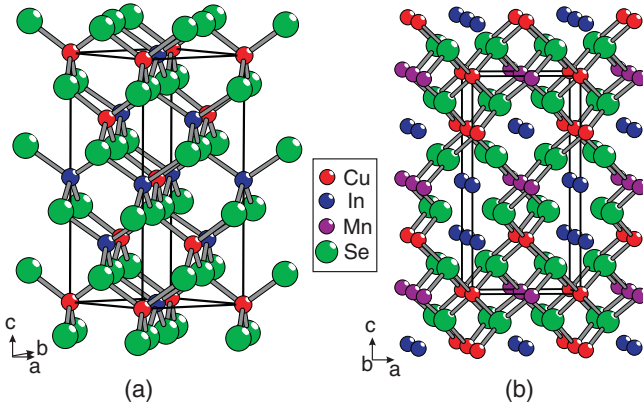


FIG. 1. (Color online) Crystal structure of $A^I B^{III} X^{VI}_2$ and Mn-substituted chalcopyrites, which are represented by (a) CuInSe_2 and (b) $(\text{Cu}_{0.75}\text{Mn}_{0.25})(\text{In}_{0.75}\text{Mn}_{0.25})\text{Se}_2$, respectively. The In-Se bonds are not shown in (b).

network an electronically conducting unit (ECU), whereas the $B^{III}-X^{VI}$ network acts as an electronically insulating unit (EIU). The structural combination of ECU and EIU in Cu-based chalcopyrites and related derivatives [Fig. 1(b)] may allow this class of compounds to possess high thermoelectric performance as shown in the $\text{Cu}_{2.1}\text{Zn}_{0.9}\text{SnSe}_4$ stannite ($ZT = 0.91$ at 860 K).¹¹

Here, in order to verify the above proposal, we chose a typical Cu-based chalcopyrite CuInSe_2 and studied its thermoelectric properties as a function of Mn substitution. It is observed that the ZT value has been enhanced by over two orders of magnitude with the introduction of Mn into the CuInSe_2 matrix, and the Seebeck coefficient S can go as high as $550 \mu\text{V K}^{-1}$. The electronic structures of the unsubstituted and Mn-substituted CuInSe_2 compounds were investigated to understand the relationship between the improvement of thermoelectric properties and the band structure changes around the Fermi level E_F due to the Mn substitution. In addition, Raman and x-ray photoelectron spectroscopy (XPS) were employed to elucidate the effects of Mn substitution on the crystal lattice and oxidation states of the constituent elements, respectively.

II. EXPERIMENTAL

A. Synthesis

1. Preparation and densification of CuInSe_2 and Mn-substituted CuInSe_2

The powder samples with a nominal composition of $\text{CuIn}_{1-x}\text{Mn}_x\text{Se}_2$ ($x = 0-0.10$) and $\text{Cu}_{1-y}\text{In}_{1-y}\text{Mn}_{2y}\text{Se}_2$ ($2y = 0.05-0.20$) were synthesized by traditional high-temperature, solid-state reactions of the constituent elements. The details of

the synthesis are described in Ref 19. These powdered samples were used for Raman and XPS studies.

Dense pellets of the synthesized materials were obtained by pressing the powders using a uniaxial hot press from Thermal Technologies Inc. The pressing was carried out under dynamic vacuum ($\sim 10^{-4}$ mbar) using a 10 mm graphite die. The pressing procedure involved heating the samples from room temperature to 600°C over 2 h, dwelling at 600°C for 1 h and cooling to room temperature over 2 h. The pressure was raised from 0 to 100 MPa over the course of 1 h, held at 100 MPa for 5 h, and released over 1 h.

The density of the samples was determined by He-gas pycnometry of the as-obtained powders, using an AccuPyc II 1340 manufactured by Micromeritics. After pressing, the samples were polished on both flat surfaces until the two sides were plane parallel. The density of the pellets was then determined by measurement of the pellet dimensions and pellet mass. The powder densities, pellet densities, and percent compaction appear in Table I. It can be seen that the density of the pellets is quite close to that of the powder samples. These dense pellets were subsequently used for the thermal conductivity, thermopower, and electrical conductivity measurements.

2. Preparation of MnSe

The MnSe powder sample was prepared by grinding a stoichiometric mixture of Mn and Se powders together and loading the mixture into a 9 mm o.d. fused-silica tube. The tube was sealed under a vacuum $< 10^{-4}$ mbar. The ampoule was heated from room temperature to 1000°C in 24 h, dwelled at 1000°C for 120 h, and cooled to room temperature in 12 h.

B. Physical measurements

1. X-ray photoelectron spectroscopy

X-ray photoelectron spectra were measured on a Kratos 165 spectrometer equipped with a monochromatic $\text{Al K}\alpha$ x-ray source (14 mA, 15 kV) and a hybrid lens with a spot size of $700 \times 400 \mu\text{m}^2$. The samples were air stable, but to minimize exposure to air, they were handled in an Ar-filled glove box where they were finely ground, pressed into In foil, mounted on a Cu sample holder, and placed in a sealed container for transfer to the analysis chamber of the spectrometer. The pressure inside the XPS instrument was maintained between 10^{-7} and 10^{-9} Pa. Samples were sputter-cleaned with an Ar^+ ion beam (4 kV, 10 mA) until core-line peaks associated with surface oxides were no longer observed in the XPS spectra. A small shoulder in the Mn $2p$ XPS spectra indicated that a slight reduction of Mn occurred during this sputtering procedure.

Survey spectra, collected with a binding energy (BE) range of 0–1100 eV with a pass energy of 160 eV, a step

TABLE I. Powder and pellet densities for $\text{CuIn}_{1-x}\text{Mn}_x\text{Se}_2$ and $\text{Cu}_{1-y}\text{In}_{1-y}\text{Mn}_{2y}\text{Se}_2$.

| Sample | CuInSe_2 | $\text{CuIn}_{0.95}\text{Mn}_{0.05}\text{Se}_2$ | $\text{CuIn}_{0.90}\text{Mn}_{0.10}\text{Se}_2$ | $\text{Cu}_{0.90}\text{In}_{0.90}\text{Mn}_{0.20}\text{Se}_2$ |
|---------------------------------------|-------------------|---|---|---|
| Powder density (g cm^{-3}) | 5.769 | 5.746 | 5.833 | 5.676 |
| Pellet density (g cm^{-3}) | 5.663 | 5.656 | 5.657 | 5.604 |
| Percent densification (%) | 98.2 | 98.4 | 97.0 | 98.7 |

TABLE II. Binding energies of the Cu 2*p*, In 3*d*, Se 3*d* and Mn 2*p* core-level photoelectron spectra for CuInSe₂, CuIn_{1-*x*}Mn_{*x*}Se₂, Cu_{1-*y*}In_{1-*y*}Mn_{2*y*}Se₂, and reference compounds.

| Compound | Mn 2 <i>p</i> _{3/2} (eV) ^a | Cu 2 <i>p</i> _{3/2} (eV) | In 3 <i>d</i> _{5/2} (eV) | Se 3 <i>d</i> _{5/2} (eV) |
|--|--|-----------------------------------|-----------------------------------|-----------------------------------|
| CuInSe ₂ | N/A | 932.7 | 445.0 | 54.3 |
| CuIn _{0.95} Mn _{0.05} Se ₂ | N/M | 932.6 | 444.9 | 54.2 |
| CuIn _{0.90} Mn _{0.10} Se ₂ | 641.3 (A), 640.1 (B), 645.0 (C) | 932.6 | 445.0 | 54.2 |
| Cu _{0.98} In _{0.98} Mn _{0.05} Se ₂ | N/M | 932.8 | 444.9 | 54.2 |
| Cu _{0.93} In _{0.93} Mn _{0.15} Se ₂ | 641.2 (A); 640.1 (B); 645.2 (C) | 932.7 | 445.0 | 54.3 |
| MnSe | 641.2 (A); 640.1 (B); 644.8 (C) | N/A | N/A | N/M |

^aBinding energies are for features A–C identified on Fig. 2.

size of 0.7 eV, and a sweep time of 180 s, confirmed the expected chemical compositions for the samples examined. High-resolution core-line spectra were collected with an energy envelope of appropriate range (60 eV for Cu; 30 eV for Mn 2*p* and In 3*d*; 20 eV for Se 3*d*), a pass energy of 20 eV, a step size of 0.05 eV, and a sweep time of 180 s. Because the Mn 2*p* core-line peak is overlapped by Cu Auger peaks, the Mn 2*p* spectra were collected with a monochromatic Mg K α x-ray source (10 mA, 15 kV) instead. Given the very low concentration of Mn in these compounds, only two of the Mn-richer members (CuIn_{0.90}Mn_{0.10}Se₂ and Cu_{0.93}In_{0.93}Mn_{0.15}Se₂) were examined. Although the compounds are semiconductors, the samples were sufficiently well conducting that no charge correction was required. The spectra were calibrated to the C 1*s* line at 284.8 eV arising from adventitious carbon. The spectra were analyzed with use of the CASAXPS software package.²⁰ The background arising from energy loss was removed by applying a Shirley-type function, and the peaks were fitted to pseudo-Voigt (70% Gaussian and 30% Lorentzian) line profiles to take into account spectrometer and lifetime broadening effects. Table II lists average BE values, with uncertainties estimated at better than ± 0.1 eV.

2. Raman spectroscopy

Raman spectra of powdered samples were recorded at 295 K from 50 to 500 cm⁻¹ at 0.6 cm⁻¹ resolution using a Horiba/Jobin Yvon LabRAM HR800 Raman microscope with a 50 mW HeNe laser source ($\lambda = 632.8$ nm). Using a confocal geometry, a 100 \times objective lens was employed for transmission of the incident laser beam and collection of the scattered radiation. Laser intensity was attenuated as necessary to prevent decomposition of the samples.

3. Thermal conductivity

The thermal conductivity (κ) of the samples was determined as a function of temperature from room temperature to 570 K, using the flash diffusivity method on an LFA 457/2/G Microflash manufactured by Netzsch. The front face of a disc-shaped specimen ($\phi \sim 10.1$ mm; thickness ~ 3.0 mm), coated on both sides with a thin layer of graphite, was irradiated by a short laser burst, and the resulting rear face temperature rise was recorded and analyzed. A standard of pyroceram was measured alongside each sample as a reference. The κ values were calculated using the equation $\kappa = \alpha C_p d$, where α is the thermal diffusivity, d is the bulk density of the sample, and C_p

is the specific heat estimated from the C_p of the pyroceram reference material measured alongside each sample.

4. Thermopower and electrical conductivity

Specimens for electronic charge transport were formed as rectangular bars with approximate dimensions of $3 \times 3 \times 9$ mm³, cut from a pellet $>97\%$ dense. These bars were cut from the same pellet used for the determination of thermal conductivity using a precision wire saw from South Bay Technology. All specimens were polished to a mirrorlike finish with SiC sandpaper using an Ecomet 3000 polisher/grinder from Buehler. Specimens were washed with ethanol and dried with acetone to remove foreign particles from the surface before measurements.

Thermopower and electrical conductivity σ data for all samples were measured simultaneously using a commercial ZEM-3 Seebeck coefficient/electrical resistivity measurement system from ULVAC-RIKO. Data were recorded in the temperature range of 300–570 K. A rectangular-shaped specimen was sandwiched between two nickel-based electrodes (current injection) with two voltage probes mechanically contacting the sample perpendicular to the flat and smoothly polished face of the specimen. The specimen, mounted on the sample holder, was then inserted into the furnace chamber, and the system was flushed several times using He gas. The measurement was performed under a residual pressure of He gas (~ 200 mbar) to facilitate homogeneous distribution of heat inside the furnace chamber. Data were collected on three heating and cooling cycles to ensure reproducibility. Since all cycles were reproducible, the data reported are the average of all three cycles.

C. Electronic structure calculations

To understand the relationship between the thermoelectronic properties and the incorporation of Mn in chalcopyrites, the calculations were performed for CuInSe₂ and a hypothetical (Cu_{0.75}Mn_{0.25})(In_{0.75}Mn_{0.25})Se₂ compound using the CASTEP package within the framework of density functional theory.²¹ For (Cu_{0.75}Mn_{0.25})(In_{0.75}Mn_{0.25})Se₂, the lattice parameters were presumed to follow Vegard's law in the Cu_{1-*y*}In_{1-*y*}Mn_{2*y*}Se₂ system,²² i.e. $a = 5.8060$ Å and $c = 11.6617$ Å. Its atomic coordinates were initially taken from those of Cu_{0.90}In_{0.90}Mn_{0.20}Se₂,¹⁹ and then the symmetry was reduced to *P*-4 to allow Mn to occupy a quarter of the Cu and In sites. The structural parameters of CuInSe₂ were taken from

the data determined by neutron and x-ray powder diffraction refinements.¹⁹ The exchange and correlation functional was treated by the generalized gradient approximation proposed by Perdew–Burke–Ernzerhof.²³ The energy cutoff for the plane-wave basis set is 350 eV, the Monkhorst–Pack scheme²⁴ for integration in the Brillouin zone was adopted, and a k -point grid of $5 \times 5 \times 6$ for CuInSe_2 and $4 \times 4 \times 2$ for $(\text{Cu}_{0.75}\text{Mn}_{0.25})(\text{In}_{0.75}\text{Mn}_{0.25})\text{Se}_2$ was determined to be precise enough for good energy convergence. The convergence tolerances for the optimization of the geometry were set as the maximum energy change within 5×10^{-6} eV/atom, the maximum ionic Hellmann–Feynman force within 0.01 eV/Å, the maximum ionic displacement within 5×10^{-4} Å, and the maximum stress within 0.02 GPa.

III. RESULTS AND DISCUSSION

A. XPS

XPS is a powerful method to directly probe the electronic structure of different elemental components within a solid. The chief ambiguity in this work pertains to the oxidation state of Mn in the Mn-substituted CuInSe_2 chalcopyrites. To this end, the Mn $2p_{3/2}$ XPS spectra for two of the Mn-richer members of the $\text{CuIn}_{1-x}\text{Mn}_x\text{Se}_2$ and $\text{Cu}_{1-y}\text{In}_{1-y}\text{Mn}_{2y}\text{Se}_2$ series were collected (Fig. 2). These spectra resemble that for a MnSe standard measured here and for MnTe reported elsewhere, where divalent Mn is present.^{25,26} Three distinct components (A–C) can be identified. (A) The main core-line peak is found at BEs ($\text{CuIn}_{0.90}\text{Mn}_{0.10}\text{Se}_2$, 641.3 eV; $\text{Cu}_{0.93}\text{In}_{0.93}\text{Mn}_{0.15}\text{Se}_2$, 641.2 eV) that are essentially identical to that in MnSe (641.2 eV). (B) The shoulder at slightly lower BE, which also plagues the spectra of MnTe and Mn oxides, results from the Ar^+ sputtering procedure.^{25–27} (C) The broad satellite at higher BE, which is found for other divalent Mn compounds, results from a shakeup process in which metal valence electrons are promoted into ligand conduction states after photoionization.²⁸ An accompanying satellite for B observed in MnTe²⁶ is presumably buried under the more intense core-line peak in the Mn-doped CuInSe_2 samples. The nature of the divalent Mn ion in CuInSe_2 has also been verified by high-frequency electron paramagnetic resonance (EPR) measurements.¹⁹

The Cu $2p$, In $3d$, and Se $3d$ XPS spectra for four members of the $\text{CuIn}_{1-x}\text{Mn}_x\text{Se}_2$ and $\text{Cu}_{1-y}\text{In}_{1-y}\text{Mn}_{2y}\text{Se}_2$ series were collected. Representative spectra for $\text{CuIn}_{0.90}\text{Mn}_{0.10}\text{Se}_2$ are shown in comparison to CuInSe_2 (Fig. 3). The qualitative observation that these spectra are unchanged indicates that Mn substitution has little or no effect on the nature of the Cu, In, and Se atoms. The Cu $2p$ XPS spectra consist of two peaks corresponding to the spin-orbit-split $2p_{3/2}$ and $2p_{1/2}$ final states in an intensity ratio of 2:1 and each with full width at half maximum (FWHM) of 1.0 eV. Although it is true that the Cu $2p_{3/2}$ BEs (932.6–932.8 eV) are typical of compounds containing Cu^+ and Cu^0 , care must be taken in interpreting these spectra because the correlation between Cu $2p_{3/2}$ BE with oxidation state is not straightforward.²⁹ The more definitive signature is an intense satellite (at 940–945 eV) above the $2p_{3/2}$ core-line peak that is characteristic for Cu^{2+} but not Cu^{1+} or Cu^0 (Two theories involving either a shakeup or a shakedown process have been proposed; both predict that the

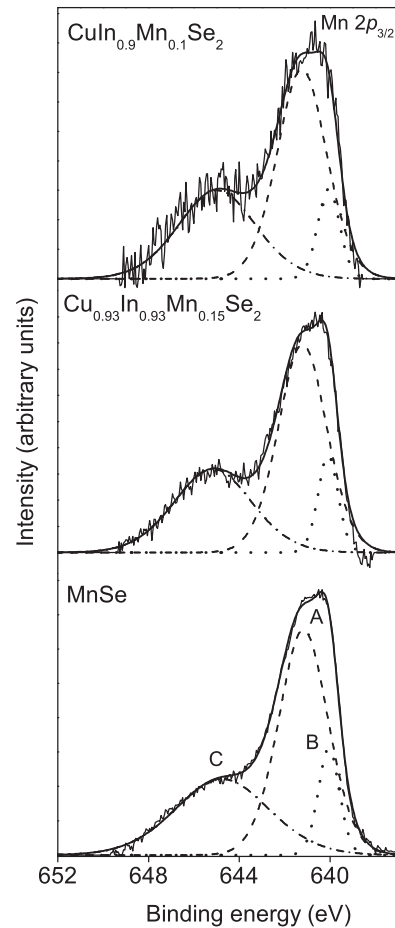


FIG. 2. Mn $2p_{3/2}$ XPS spectra of $\text{CuIn}_{0.90}\text{Mn}_{0.10}\text{Se}_2$, $\text{Cu}_{0.93}\text{In}_{0.93}\text{Mn}_{0.15}\text{Se}_2$ and MnSe. Thin solid line = experimental spectrum, thick solid line = spectrum obtained by nonlinear least-square fit with use of three pseudo-Voigt singlets. The underlying singlet components that comprise the above peak envelope were denoted as follows: A = dashes, B = dots, C = dash dots.

satellite is only possible for Cu^{2+} where empty $3d$ conduction states are available).^{30,31} The absence of such a satellite and the resemblance of the spectra to those of copper(I) halides (e.g. CuBr , CuI)^{32,33} confirms the presence of Cu^+ . The In $3d_{5/2}$ BE in $\text{CuIn}_{0.90}\text{Mn}_{0.10}\text{Se}_2$ and CuInSe_2 (445.0 eV) is higher than in elemental In [443.8(3) eV] but similar to that in In_2O_3 [444.8(4) eV],³⁴ indicating the presence of positively

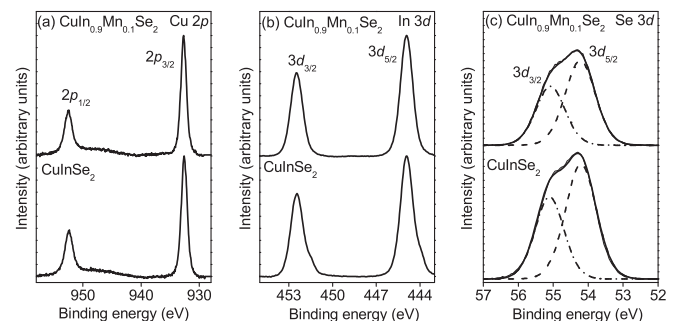


FIG. 3. XPS spectra of (a) Cu $2p$, (b) In $3d$, and (c) Se $3d$ for $\text{CuIn}_{0.90}\text{Mn}_{0.10}\text{Se}_2$ and CuInSe_2 .

charged In³⁺ species. The Se 3*d* XPS spectra each show one broad signal, fitted to 3*d*_{5/2} and 3*d*_{3/2} components, with an intensity ratio of 3:2, FWHM of 1.0 eV, and a splitting of 0.85 eV. The Se 3*d*_{5/2} BE in CuIn_{0.90}Mn_{0.10}Se₂ and CuInSe₂ (54.3 eV) is lower than in elemental Se [55.4(7) eV],³⁴ consistent with anionic Se.

B. Raman spectroscopy

The Raman spectrum of CuInSe₂ [Fig. 4(a)] is consistent with the chalcopyrite structure and dominated by an intense A₁ phonon signal at 170 cm⁻¹.³⁵ Smaller signals corresponding to E (210 cm⁻¹) and B₂ (225 cm⁻¹) phonon modes are also observed. Substitution with increasing levels of Mn results in the lowering of signal-to-noise ratio and the emergence of new signals at 125 and 255 cm⁻¹ with a corresponding decrease in relative A₁ phonon signal intensity [Figs. 4(b)–4(e)].

The substitution of Mn for In in CuIn_{1-x}Mn_xSe₂ samples and for Cu and In in Cu_{1-y}In_{1-y}Mn_{2y}Se₂ samples has little effect on A₁ phonon signal frequency. For the range of Mn substitution studied (0 < *x* < 0.10 and 0 < 2*y* < 0.15), this phonon frequency remains at 170 ± 2 cm⁻¹ with no discernable trend in position shift regardless of Mn content. This result is consistent with the minimal changes in lattice parameters we have reported for these levels of Mn substitution [for 0 < *x* < 0.10: *a* = 5.7842(1) to 5.7893(1) Å and *c* = 11.6266(3) to 11.6340(3) Å; for 0 < 2*y* < 0.15: *a* = 5.7842(1) to 5.7924(1) Å and *c* = 11.6266(3) to 11.6353(5) Å].²²

An increase in crystalline disorder is apparent with greater amounts of Mn. In addition to lower signal-to-noise ratio, this is evidenced by the emergence of a broad phonon signal at 255 cm⁻¹ that is likely due to surface Cu_{2-x}Se phases that have separated from the bulk chalcopyrite material³⁶ as well as increased intensity of a 125 cm⁻¹ phonon. This signal is the most prominent feature of the Cu_{1-y}In_{1-y}Mn_{2y}Se₂ spectra. Low-intensity 124 cm⁻¹ phonon signals have been observed^{35,37} in CuInSe₂ and assigned to a B₁ vibrational mode³⁵ due to cation antiphase motion.³⁸ Such dramatic enhancement of this mode through lattice substitution of one or both metal ions seems unlikely. Uniform substitution

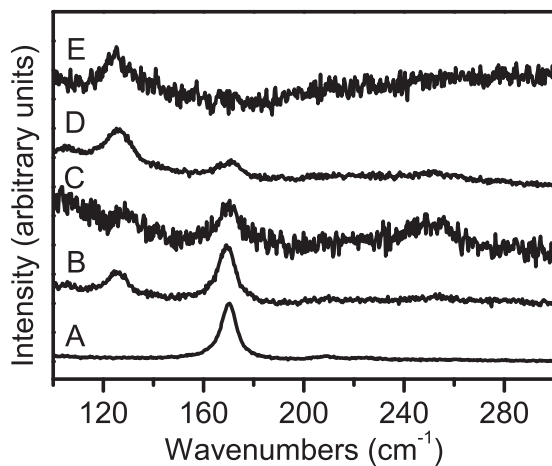


FIG. 4. Raman spectra of CuInSe₂, CuIn_{1-x}Mn_xSe₂ and Cu_{1-y}In_{1-y}Mn_{2y}Se₂ samples: (A) CuInSe₂; (B) *x* = 0.05; (C) *x* = 0.10; (D) 2*y* = 0.05; and (E) 2*y* = 0.15.

would maintain the chalcopyrite symmetry properties, while nonuniform substitution would lead to phase separation that would be evident in Raman spectra and x-ray powder diffraction patterns. For example, Raman spectra of bulk crystal, nanocrystalline, and thin-film CuIn_{1-x}M_xSe₂ (*M* = Ga, Al) throughout 0 < *x* < 1 composition ranges³⁹⁻⁴¹ have not resulted in such increases in the B₁ mode signal intensity. Some identified Cu_{2-x}Se phase separation is observed at 255 cm⁻¹ [Fig. 4(c)]; however, the 125 cm⁻¹ phonon in Figs. 4(b)–4(e) does not correspond to signals for reported amorphous or crystalline indium selenide or manganese selenide phases.⁴²⁻⁴⁶

It is possible that Mn substitution introduces local disorder in the crystal lattice resulting in a vibrational imbalance that could give rise to an intense acoustic phonon signal in the 125 cm⁻¹ region. Some ternary zinc blende systems of the form A_{1-x}B_xC (*A* and *B* = cations; *C* = chalcogenide anion) are known to exhibit impurity-induced vibrational modes that have been proposed to consist of symmetric breathing motion of anions about a nearest neighbor cation impurity. Formally labeled defect-activated longitudinal acoustic (DALA) and defect-activated transverse acoustic (DATA) vibrational modes⁴⁷ have been observed to be largely independent of cation and anion atomic mass as evidenced in Zn_{1-x}Mn_xTe (120 cm⁻¹), Cd_{1-x}Mg_xTe (119 cm⁻¹), and Cd_{1-x}Mn_xTe (112 cm⁻¹).⁴⁸⁻⁵⁰ Should the 125 cm⁻¹ phonon in Fig. 4 stem from a DALA or DATA vibrational mode, the greater intensity of this signal in Cu_{1-y}In_{1-y}Mn_{2y}Se₂ samples compared to CuIn_{1-x}Mn_xSe₂ samples would imply that there is greater impurity-induced disorder in the former. However, this is difficult to conclude, as our neutron powder diffraction studies¹⁹ indicate that in both types of samples, Mn ions are distributed in both Cu and In lattice sites.

C. Thermoelectric properties and electronic structure

1. Thermal conductivity

The temperature dependence of total thermal conductivity is shown in Fig. 5. All samples exhibit a relatively low κ , e.g. 1.6–1.9 W m⁻¹ K⁻¹ at 560 K, compared to those of well-known thermoelectric materials.^{13,15-18} As known, κ is the sum of the electronic thermal conductivity κ_e and the lattice thermal conductivity κ_L . Here, κ_e was estimated from the electrical conductivity using the Wiedemann–Franz law, $\kappa_e = \sigma LT$, where the Lorenz number *L* was assumed to be 2.44 × 10⁻⁸ W Ω K⁻², an appropriate value for degenerate systems. In this manner, κ_e is estimated to be smaller than 1% of the total κ in the whole range of temperatures studied, indicating that the thermal vibration of the lattice provides the dominant scattering mechanism for charge carriers. For all the samples, κ is inversely proportional to temperature, indicating that the thermal transport is dominated by acoustic phonon scattering.¹²

Here, κ and κ_L are suppressed slightly by the introduction of Mn into CuInSe₂, mostly due to the lattice disordering by the Mn substitution (Fig. 5). Our structural analysis reveals that Mn occupies both cation sites with the preference of Mn occupation on the Cu site Mn_{Cu} and the presence of antisite Cu_{In} defects,¹⁹ increasing the degree of lattice disorder and thus diminishing the thermal conductivity. The degree of lattice

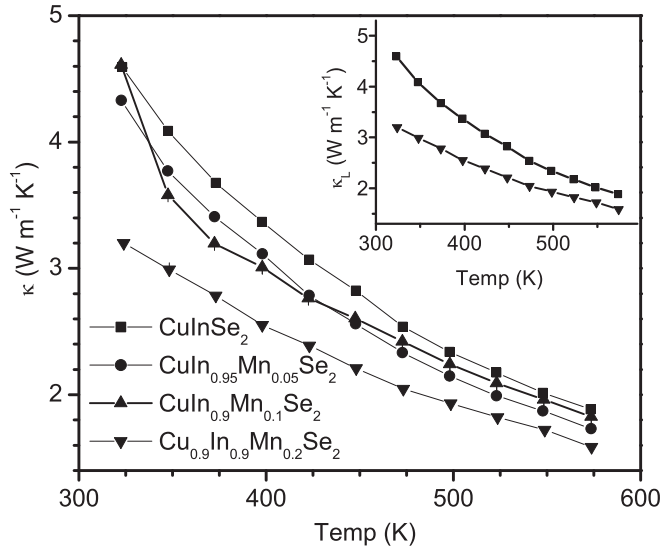


FIG. 5. Temperature dependence of thermal conductivity for unsubstituted and Mn-substituted CuInSe₂. Inset shows the lattice thermal conductivity as a function of temperature of the samples. For clarity, only the data of CuInSe₂ and Cu_{0.90}In_{0.90}Mn_{0.20}Se₂ are shown.

disorder is also supported by the Raman measurements on our Mn-substituted samples.

2. Electrical conductivity

Figure 6 shows σ for CuInSe₂ and the Mn-substituted CuInSe₂ compounds as a function of temperature from 300 to 550 K. CuInSe₂ shows a small σ of 0.12 S cm⁻¹ at room temperature within the reported range of 0.005–300 S cm⁻¹ for bulk CuInSe₂ compounds.⁵¹ It can be seen that σ for

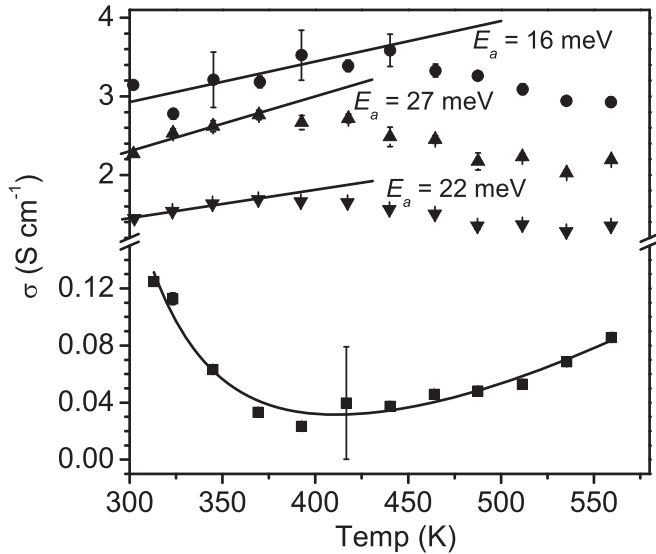


FIG. 6. Temperature dependence of electrical conductivity for CuInSe₂ (■), CuIn_{0.95}Mn_{0.05}Se₂ (●), CuIn_{0.90}Mn_{0.10}Se₂ (▲), and Cu_{0.90}In_{0.90}Mn_{0.20}Se₂ (▼). The solid curve is a fit for CuInSe₂ data using Eq. (1) with $m = 8.6$ and $E_a = 0.195$ eV, $\sigma_M = 3.24 \times 10^{20}$ S cm⁻¹, $\sigma_S = 4.77$ S cm⁻¹. The linear solid lines are fit for data of the Mn-substituted samples using $\sigma = \sigma_0 \exp[-E_a/(k_B T)]$.

our CuInSe₂ sample has a minimum at ~ 390 K while σ for Mn-substituted CuInSe₂ materials increases by over an order of magnitude and exhibits a weak temperature dependence. Overall, σ of all the samples is smaller than Mott's minimum metallic conductivity $\sigma_{\min} = e^2/(3\hbar a)$, where e denotes the electron charge, \hbar represents the rationalized Planck's constant, and a is the distance between atoms.⁵² Given $a \approx 3$ Å in the chalcopyrites, $\sigma_{\min} \approx 260$ S cm⁻¹ which is substantially larger than the σ of our samples (Fig. 6), suggesting that the synthesized materials are not typical metallic materials. Considering an evident band gap ($E_g \sim 0.90$ eV) for all the samples measured using optical diffuse reflectance spectra,²² the samples are believed to be semiconductors, even though they exhibit metal-like behavior with respect to σ at some temperature intervals.

For the unsubstituted CuInSe₂ compound, σ displays metal-like behavior at temperatures lower than ~ 390 K, and then it shows semiconducting behavior at higher temperatures (Fig. 7). In the corresponding temperature intervals, S behaves similarly. That is, $S > 0$ suggests that its conductivity is p -type up to 392 K, and then S changes to a downward trend and becomes negative (n -type conductivity) above 500 K (Fig. 6). According to our crystal structure analysis based on x-ray diffraction and neutron data, the unsubstituted CuInSe₂ compound is Cu poor and Se poor, indicating the existence of copper V_{Cu} and selenium V_{Se} vacancies.¹⁹ The V_{Cu} and V_{Se} defects act as acceptors and donors, respectively. According to the theoretical and experimental work, V_{Cu} form the shallowest acceptor level with an ionization energy around 30–40 meV and V_{Se} have an ionization energy of 120–260 meV.^{53,54} Therefore the electrical conduction mechanism for CuInSe₂ can be seen as two-charge carrier behavior, p -type V_{Cu} and n -type V_{Se} . Because of the small ionization energy of V_{Cu} , the acceptor state is completely ionized at $T > 300$ K, and σ is determined primarily by the variation of mobility μ with temperature according to $\mu \propto T^{-m}$. The hole mobility is attenuated upon heating due to the lattice and impurity scattering, resulting in the metal-type behavior lower than 392 K. When the temperature increases further, the V_{Se} donor state is activated and compensates the V_{Cu} acceptor state, leading to the n -type conduction. Based on this assessment, the thermal behavior of σ can be fitted by the following equation:

$$\sigma = \sigma_M T^{-m} + \sigma_S \exp\left(-\frac{E_a}{k_B T}\right) \quad (1)$$

where σ_M and σ_S are prefactors, m is a scattering coefficient, T is the absolute temperature, E_a is activation energy, and k_B is the Boltzmann's constant. The fit to the data employing Eq. (1) gives $m = 8.6$ and $E_a = 195$ meV, which is in the range of 120–260 meV for the V_{Se} activation energy reported in the literature.⁵⁴

In Fig. 6, one can see that σ of the Mn-substituted samples is one order of magnitude greater than that of CuInSe₂, and the conductivity is p -type. The oxidation states of the cations are Cu⁺, In³⁺, and Mn²⁺ verified by the above XPS measurements and previous EPR measurements¹⁹ of these samples. Therefore, the replacement of Mn for In introduces a hole in the electrical conduction, which increases the charge carrier concentration n and thus essentially results in the enhancement of electrical conductivity based on the equation

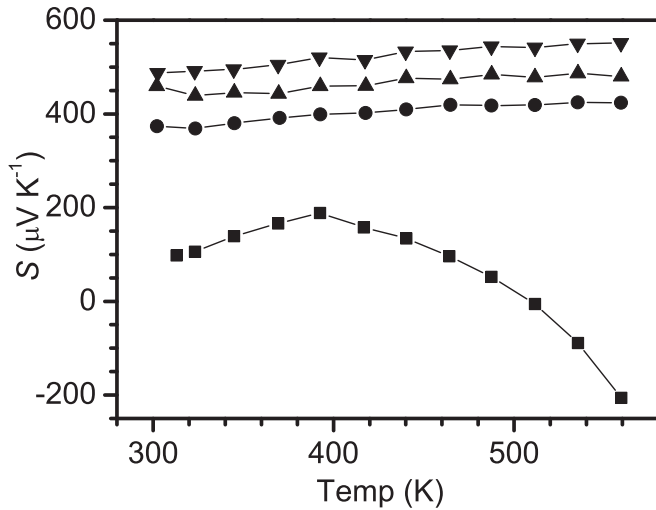


FIG. 7. Temperature dependence of Seebeck coefficient for CuInSe₂ (■), CuIn_{0.95}Mn_{0.05}Se₂ (●), CuIn_{0.90}Mn_{0.10}Se₂ (▲), and Cu_{0.90}In_{0.90}Mn_{0.20}Se₂ (▼).

$\sigma = ne\mu$. The decrease of σ with increasing Mn content may be due to the increase in the number of scattering centers.

For the Mn-substituted samples, σ increases smoothly with rising temperature up to ~ 400 K and then decreases with further increase in temperature. A small activation energy of $E_a = 16\text{--}27$ meV is fitted from the semiconducting conductivity data at 300–400 K. This E_a is smaller than the activation energy of any donors and acceptors in undoped CuInSe₂ ($E_a = 30\text{--}40$ meV for the shallowest V_{Cu} level).^{53,54} Such a small E_a may be related to the Mn-substituted extrinsic acceptors, e.g. Mn on the In site Mn_{In} , or grain boundary barriers.

3. Seebeck coefficient and figure of merit

The Seebeck effect as a function of temperature for all the samples is shown in Fig. 7. At room temperature, S for all the samples is positive, suggesting that the materials are *p*-type semiconductors. For the unsubstituted CuInSe₂ compound, $S \sim 100 \mu\text{V K}^{-1}$ at 330 K. This is comparable to the Seebeck effect of typical thermoelectric materials (see Table III),^{13,15,16,18} and may be due to its relatively wide band

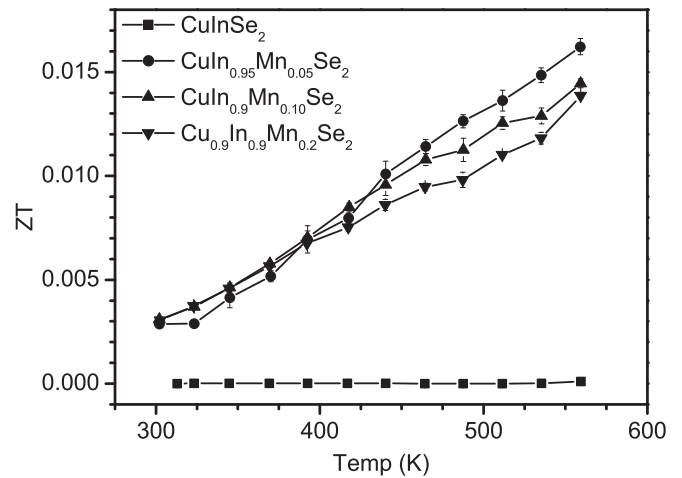


FIG. 8. Temperature dependence of ZT for CuInSe₂ and Mn-substituted CuInSe₂.

gap. As discussed above, the electronic transport of CuInSe₂ is a two-charge carrier behavior, i.e. *p*-type V_{Cu} dominating lower than 392 K and *n*-type V_{Se} dominating at temperatures higher than 392 K. The corresponding behavior can be observed in the Seebeck effect of CuInSe₂, that is, S is significantly suppressed at temperatures higher than 392 K due to electrons and holes having opposite charges, and S becoming negative when *n*-type V_{Se} dominates the electrical conduction at high temperatures.

Interestingly, the introduction of Mn into the CuInSe₂ matrix enhances S by a factor of ~ 4 compared to that of CuInSe₂, for example, $S = 480 \mu\text{V K}^{-1}$ at 300 K for Cu_{0.90}In_{0.90}Mn_{0.20}Se₂. The improvement of the Seebeck coefficient perhaps arises from a local increase in the densities of states (DOS) near E_F . The monotonic increase of S for the Mn-substituted CuInSe₂ chalcopyrites with temperature (Fig. 7), as well as the weak temperature dependence of σ demonstrated above (Fig. 6), indicates that the Mn-substituted samples are degenerate semiconductors. Degenerate semiconducting behavior can often be observed in heavily doped semiconductors.¹⁴

The performance of a thermoelectric material is evaluated by the dimensionless figure of merit ZT as $ZT = \sigma S^2 T / \kappa$. The

TABLE III. High-temperature thermoelectric properties of CuInSe₂ and Mn-substituted CuInSe₂ compounds, compared to those of some bulk state-of-the-art thermoelectric materials.

| Material | T (K) | σ (S cm ⁻¹) | S ($\mu\text{V K}^{-1}$) | κ (W m ⁻¹ K ⁻¹) | ZT |
|--|------------|--------------------------------|------------------------------|---|----------------------|
| CuInSe ₂ | 560 | 0.09 | -206 | 1.9 | 1.1×10^{-4} |
| CuIn _{0.95} Mn _{0.05} Se ₂ | 560 | 2.9 | 424 | 1.8 | 1.6×10^{-2} |
| CuIn _{0.90} Mn _{0.10} Se ₂ | 560 | 2.2 | 480 | 1.8 | 1.4×10^{-2} |
| Cu _{0.90} In _{0.90} Mn _{0.20} Se ₂ | 560 | 1.4 | 551 | 1.6 | 1.4×10^{-2} |
| Bi ₂ Te _{2.7} Se _{0.3} ^a | ~ 300 | 1000 | -210 | 1.4 | 0.9 |
| Tl _{0.02} Pb _{0.98} Te ^b | 773 | 16667 | 335 | 0.98 | 1.47 |
| LaFe ₃ CoSb ₁₂ ^c | 800 | 454 | 200 | 1.6 | 0.9 |
| AgPb ₁₈ SbTe ₂₀ ^d | 800 | 250 | -335 | 1.1 | 2.1 |

^aReference 18.

^bReference 15.

^cReference 13.

^dReference 16.

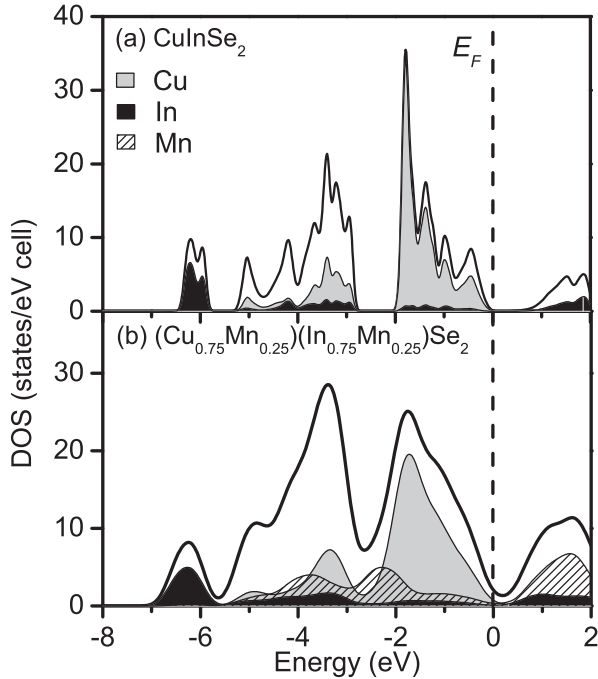


FIG. 9. Total and projected densities of states (DOS) of (a) CuInSe_2 and (b) antiferromagnetic $(\text{Cu}_{0.75}\text{Mn}_{0.25})(\text{In}_{0.75}\text{Mn}_{0.25})\text{Se}_2$.

ZT , as well as other properties of CuInSe_2 and Mn-substituted CuInSe_2 , is gathered in Table III, and the thermoelectric performance of typical thermoelectric materials is also listed in this table for comparison.^{13,15–18} Owing to the suppression of κ and the enhancement of σ and S by the Mn substitution, the ZT of the Mn-substituted CuInSe_2 is enhanced by over two orders of magnitude (Fig. 8). The small ZT (<0.02) makes these materials of little interest for practical thermoelectric applications (typically $ZT > 1$) due to the ultralow σ . However, the strong enhancement of ZT in these chalcopyrites upon Mn substitution is rather surprising. This observation accompanied by the reported sizable thermoelectric performance of cation-mixed $\text{Cu}_{2+x}\text{A}^{\text{II}}_{1-x}\text{SnX}^{\text{VI}}_4$ ($\text{A}^{\text{II}} = \text{Zn, Cd}$ and $\text{X}^{\text{VI}} = \text{S, Se}$) stannites at high temperatures¹¹ suggests that transition-metal-substituted, Cu-based ternary/quaternary diamond-like semiconductors may be viable thermoelectric candidates.

4. Electronic structure

In order to elucidate the origin of the enhanced thermoelectric properties by the Mn substitution in the CuInSe_2 and related diamond-like semiconductors, the band structures of CuInSe_2 and the hypothetical $(\text{Cu}_{0.75}\text{Mn}_{0.25})(\text{In}_{0.75}\text{Mn}_{0.25})\text{Se}_2$ compound were calculated (Fig. 9). For CuInSe_2 [Fig. 9(a)], its CBM is an antibonding combination of In $5s$ -Se $4p$ states, whereas the VBM (-2 – 0 eV) is a mixed state derived from Cu $3d$ and Se $4p$ orbitals. The states located between -5.3 and -2.7 eV mainly come from the bonding Cu $3d$ -Se $4p$ and In $5p$ -Se $4p$ bands. The lowest lying energy states from -6.5 to -5.7 eV are a hybridization of In $5s$ and Se $4p$ orbitals. Similar band structures of chalcopyrite semiconductors can be found elsewhere.^{4,6,7}

Three magnetic states, paramagnetic, ferromagnetic, and antiferromagnetic (AFM), were assigned for the calculations of $(\text{Cu}_{0.75}\text{Mn}_{0.25})(\text{In}_{0.75}\text{Mn}_{0.25})\text{Se}_2$. In the AFM model, the magnetic moment of Mn_{Cu} aligns antiparallel to that of Mn_{In} . It turns out that the AFM state is more stable than the paramagnetic one by 3.49 eV and the ferromagnetic one by 0.06 eV, respectively. Thus the following analysis of electronic structure for $(\text{Cu}_{0.75}\text{Mn}_{0.25})(\text{In}_{0.75}\text{Mn}_{0.25})\text{Se}_2$ is carried out on the AFM model. It should be noted that the Mn content in $(\text{Cu}_{0.75}\text{Mn}_{0.25})(\text{In}_{0.75}\text{Mn}_{0.25})\text{Se}_2$ is far greater than that in our actual Mn-substituted CuInSe_2 samples,^{19,22} therefore, the changes in the band structure due to the introduction of Mn shall be qualitatively analyzed. When Mn is incorporated in CuInSe_2 , a portion of the Mn occupies the In site Mn_{In} .¹⁹ It is expected that the Mn_{In} occupation generates holes close to the VBM, moving E_F into the acceptor level and thus increasing the DOS in the vicinity of E_F . This simple reasoning is supported by the band structure calculations of $(\text{Cu}_{0.75}\text{Mn}_{0.25})(\text{In}_{0.75}\text{Mn}_{0.25})\text{Se}_2$. It can be seen that the E_F falls in the top region of the valence band and a finite DOS presence around E_F , resulting in the metallic behavior of the Mn-containing samples and the enhancement of σ and thus ZT . The DOS in the proximity of the E_F comes mainly from the Cu $3d$, Mn $3d$, and Se $4p$ states, suggesting that the interconnected Cu-Se and Mn-Se networks can provide a conduction pathway for charge carriers [Fig. 1(b)].

As stated above and in the electronic structure studies of $\text{A}^{\text{I}}\text{B}^{\text{III}}\text{X}^{\text{VI}}_2$ chalcopyrites,^{4,6,7} the chalcopyrite semiconductors present similar features in the band structures: (i) the hybridization of $\text{A}^{\text{I}} d$ - $\text{X}^{\text{VI}} p$ orbitals significantly contributes to the upper valence band, which provides the conduction pathway for charge carriers in the p -type semiconductors; and (ii) simultaneously, the weak hybridization of $\text{B}^{\text{III}}-\text{X}^{\text{VI}}$ orbitals is located deep in the valence band and in the conduction band,^{4,6,7} rendering the $\text{B}^{\text{III}}-\text{X}^{\text{VI}}$ network as an EIU. The deliberate introduction of transition metals (TM), e.g. Ti, V, Cr, and Mn, into the $\text{A}^{\text{I}}\text{B}^{\text{III}}\text{X}^{\text{VI}}_2$ chalcopyrites can enhance σ and S by inducing sharp impurity states around the E_F and also increase the phonon scattering by introducing crystallographic disorder. Therefore, the TM-substituted $\text{A}^{\text{I}}\text{B}^{\text{III}}\text{X}^{\text{VI}}_2$ chalcopyrites can be seen as an assembly of interpenetrating ECU [$\text{A}^{\text{I}}-\text{X}^{\text{VI}}$]/[TM- X^{VI}] and EIU [$\text{B}^{\text{III}}-\text{X}^{\text{VI}}$] networks [Fig. 1(b)], which is possibly a new guide to developing novel thermoelectric materials.¹¹

IV. CONCLUSION

In summary, the improvement in thermoelectric properties for $\text{CuB}^{\text{III}}\text{X}^{\text{VI}}_2$ chalcopyrites has been achieved by the introduction of Mn. The previous structural analysis of Mn-substituted CuInSe_2 revealed that Mn occupies both the Cu and In sites with a preferred occupation of Mn_{Cu} , and greater Mn content tends to distribute more evenly on both cation sites.¹⁹ This means the Mn substitution introduces lattice disorder into the parent compound, which was verified by the Raman studies presented here, leading to the reduction of κ . The Mn substitution significantly changes the band structure of these materials. The Mn_{B} occupation generates holes, and the Mn $3d$ level hybridization with the $\text{X}^{\text{VI}} np$ level

results in the finite DOS around E_F ,⁸ leading to a significant enhancement of S and σ for Mn-substituted $\text{CuB}^{\text{III}}\text{X}^{\text{VI}}_2$ chalcopyrites.

The thermoelectric studies of Mn-substituted CuInSe₂, as well as recent studies of Cu-doped $\text{Cu}_{2+x}\text{A}^{\text{II}}_{1-x}\text{SnX}^{\text{VI}}_4$ ($\text{A}^{\text{II}} = \text{Zn, Cd}$ and $\text{X}^{\text{VI}} = \text{S, Se}$) stannites,¹¹ open a new route to high- ZT materials with relatively wide band gaps and a combination of electronically conducting and insulating units. The significant finding of this study is that the TM substitution can significantly optimize the thermoelectric parameters, whereas the improvement of one of these properties is usually at the cost of the other for many other thermoelectric materials.^{12,13,16} This work, therefore, encourages us to use TM substitution into ternary-quaternary diamond-like semiconductors with high σ , such as CuTiTe_2 and $\text{A}^{\text{I}_2}\text{A}^{\text{II}}\text{B}^{\text{IV}}\text{X}^{\text{VI}}_4$ stannites, to search for new thermoelectric materials.

ACKNOWLEDGMENTS

This work was supported by the National Science Foundation CAREER Award under Grant No. DMR-0645304 and the US Department of Energy Grant No. DE-FG36-08GO88007. This work made use of the laser flash diffusivity apparatus (LFA4-57) purchased with funds from the Louisiana Board of Regents [Grant No. LEQSF(2008-09)-ENH-TR-58] (awarded to P.F.P.P.). N.J.T. and P.F.P.P. thank DARPA (Grant No. HR0011-08-1-0084) for financial support. A.M. and P.E.R.B. thank the Natural Sciences and Engineering Research Council, Alberta Ingenuity, and the University of Alberta for research and scholarship support. Access to the Kratos AXIS 165 XPS spectrometer was provided by the Alberta Centre for Surface Engineering and Science, which was established with support from the Canada Foundation for Innovation and Alberta Innovation and Science.

*aitkenj@duq.edu

¹B. J. Stanbery, *Crit. Rev. Solid State Mater. Sci.* **27**, 73 (2002).

²D. M. Gruen and I. Buckley-Golder, *MRS Bull.* **23**, 16 (1998).

³J. L. Shay and J. H. Wernick, *Ternary Chalcopyrite Semiconductors: Growth, Electronic Properties, and Applications* (Pergamon, New York, 1975), p. 3–34.

⁴J. E. Jaffe and A. Zunger, *Phys. Rev. B* **28**, 5822 (1983).

⁵J. L. Shay, B. Tell, H. M. Kasper, and L. M. Schiavone, *Phys. Rev. B* **5**, 5003 (1972).

⁶J. E. Jaffe and A. Zunger, *Phys. Rev. B* **27**, 5176 (1983).

⁷J. E. Jaffe and A. Zunger, *Phys. Rev. B* **29**, 1882 (1984).

⁸Y. J. Zhao and A. J. Freeman, *J. Magn. Magn. Mater.* **246**, 145 (2002).

⁹S. Picozzi, Y. J. Zhao, A. J. Freeman, and B. Delley, *Phys. Rev. B* **66**, 205206 (2002).

¹⁰Y. J. Zhao and A. Zunger, *Phys. Rev. B* **69**, 104422 (2004).

¹¹M. L. Liu, I. W. Chen, F. Q. Huang, and L. D. Chen, *Adv. Mater.* **21**, 3808 (2009).

¹²G. A. Slack, *CRC Handbook of Thermoelectrics*, edited by D. M. Rowe, Chapter 3 (CRC Press, Boca Raton, FL, 1995), p. 407.

¹³B. C. Sales, D. Mandrus, and R. K. Williams, *Science* **272**, 1325 (1996).

¹⁴G. S. Nolas, J. L. Cohn, G. A. Slack, and S. B. Schujman, *Appl. Phys. Lett.* **73**, 178 (1998).

¹⁵J. P. Heremans, V. Jovovic, E. S. Toberer, A. Saramat, K. Kurosaki, A. Charoenphakdee, S. Yamanaka, and G. J. Snyder, *Science* **321**, 554 (2008).

¹⁶K. F. Hsu, S. Loo, F. Guo, W. Chen, J. S. Dyck, C. Uher, T. Hogan, E. K. Polychroniadis, and M. G. Kanatzidis, *Science* **303**, 818 (2004).

¹⁷S. Ohta, T. Nomura, H. Ohta, M. Hirano, H. Hosono, and K. Koumoto, *Appl. Phys. Lett.* **87**, 092108 (2005).

¹⁸G. S. Nolas, J. Sharp, and H. J. Goldsmid, *Thermoelectrics: Basic Principles and New Materials Developments* (Springer, New York, 2001), p. 111-130.

¹⁹J. Yao, Z. Wang, J. van Tol, N. S. Dalal, and J. A. Aitken, *Chem. Mater.* **22**, 1647 (2010).

²⁰N. Fairley, *Casa Software Ltd.* (Teignmouth, Devon, UK, 2003).

²¹M. D. Segall, P. J. D. Lindan, M. J. Probert, C. J. Pickard, P. J. Hasnip, S. J. Clark, and M. C. Payne, *J. Phys.: Condens. Matt.* **14**, 2717 (2002).

²²J. Yao, C. N. Kline, H. Gu, M. Yan, and J. A. Aitken, *J. Solid State Chem.* **182**, 2579 (2009).

²³J. P. Perdew, K. Burke, and M. Ernzerhof, *Phys. Rev. Lett.* **77**, 3865 (1996).

²⁴H. J. Monkhorst and J. D. Pack, *Phys. Rev. B* **13**, 5188 (1976).

²⁵R. J. Iwanowski, M. H. Heinonen, and E. Janik, *Appl. Surf. Sci.* **249**, 222 (2005).

²⁶R. J. Iwanowski, M. H. Heinonen, and E. Janik, *Chem. Phys. Lett.* **387**, 110 (2004).

²⁷O. Giraldo, S. L. Brock, W. S. Willis, M. Marquez, S. L. Suib, and S. Ching, *J. Am. Chem. Soc.* **122**, 9330 (2000).

²⁸M. A. Brisk and A. D. Baker, *J. Electron Spectrosc. Relat. Phenom.* **7**, 197 (1975).

²⁹D. C. Frost, A. Ishitani, and C. A. McDowell, *Mol. Phys.* **24**, 861 (1972).

³⁰P. C. Healy, S. Myhra, and A. M. Stewart, *Jpn. J. Appl. Phys., Part 2* **26**, L1884 (1987).

³¹S. K. Chawla, N. Sankarraman, and J. H. Payer, *J. Electron Spectrosc. Relat. Phenom.* **61**, 1 (1992).

³²R. P. Vasquez, *Surf. Sci. Spectra* **2**, 144 (1993).

³³R. P. Vasquez, *Surf. Sci. Spectra* **2**, 149 (1993).

³⁴C. D. Wagner, A. V. Naumkin, A. Kraut-Vass, J. W. Allison, C. J. Powell, and J. R. Rumble Jr., *The Measurement Services Division of the National Institute of Standards and Technology*, 2003.

³⁵C. Rincon and F. J. Ramirez, *J. Appl. Phys.* **72**, 4321 (1992).

³⁶V. Izquierdo-Roca, A. Perez-Rodriguez, A. Romano-Rodriguez, J. R. Morante, J. Alvarez-Garcia, L. Calvo-Barrio, V. Bermudez, P. P. Grand, O. Ramdani, L. Parissi, and O. Kerrec, *J. Appl. Phys.* **101**, 103517 (2007).

³⁷E. P. Zaretskaya, V. F. Gremenok, V. Riede, W. Schmitz, K. Bente, V. B. Zaleski, and O. Ermakov, *J. Phys. Chem. Solids* **64**, 1989 (2003).

³⁸F. W. Ohrendorf and H. Haeuseler, *Cryst. Res. Technol.* **34**, 351 (1999).

³⁹W. Gebicki, M. Igalson, W. Zajac, and R. Trykozko, *J. Phys. D: Appl. Phys.* **23**, 964 (1990).

- ⁴⁰J. Olejníček, C. A. Kamler, A. Mirasano, A. L. Martinez-Skinner, M. A. Ingersoll, C. L. Exstrom, S. A. Darveau, J. L. Huguenin-Love, M. Diaz, N. J. Ianno, and R. J. Soukup, *Sol. Energy Mater. Sol. Cells* **94**, 8 (2010).
- ⁴¹J. Olejníček, L. E. Slaymaker, A. R. Vandeventer, C. L. Exstrom, S. A. Darveau, C. A. Kamler, N. J. Ianno, and R. J. Soukup, (unpublished).
- ⁴²K. Kambas, C. Julien, M. Jouanne, A. Likforman, and M. Guittard, *Phys. Status Solidi B* **124**, K105 (1984).
- ⁴³S. Marsillac, A. M. Combot-Marie, J. C. Bernède, and A. Conan, *Thin Solid Films* **288**, 14 (1996).
- ⁴⁴J. Weszka, P. Daniel, A. Burian, A. M. Burian, and A. T. Nguyen, *J. Non-Cryst. Solids* **265**, 98 (2000).
- ⁴⁵J. Weszka, P. Daniel, A. M. Burian, A. Burian, M. Elechower, and A. T. Nguyen, *J. Non-Cryst. Solids* **315**, 219 (2003).
- ⁴⁶A. Milutinovic, Z. V. Popovic, N. Tomic, and S. Devic, *Mater. Sci. Forum* **453-454**, 299 (2004).
- ⁴⁷D. N. Talwar, M. Vandevyver, and M. Zigone, *J. Phys. C: Solid State Phys.* **13**, 3775 (1980).
- ⁴⁸D. L. Peterson, A. Petrou, W. Girit, A. K. Ramdas, and S. Rodriguez, *Phys. Rev. B* **33**, 1160 (1986).
- ⁴⁹S. Nakashima, T. Fukumoto, A. Mitsuishi, and K. Itoh, *J. Phys. Soc. Jpn.* **35**, 1437 (1973).
- ⁵⁰S. Venugopalan, A. Petrou, R. R. Galazka, A. K. Ramdas, and S. Rodriguez, *Phys. Rev. B* **25**, 2681 (1982).
- ⁵¹R. R. Philip, B. Pradeep, G. S. Okram, and V. Ganesan, *Semicond. Sci. Technol.* **19**, 798 (2004).
- ⁵²N. F. Mott, *Philos. Mag.* **26**, 1015 (1972).
- ⁵³S. B. Zhang, S. H. Wei, A. Zunger, and H. Katayama-Yoshida, *Phys. Rev. B* **57**, 9642 (1998).
- ⁵⁴C. Rincon and R. Marquez, *J. Phys. Chem. Solids* **60**, 1865 (1999).